

Direct Numerical Simulation of Preignition and Knock in Engine Conditions



Minh Bau Luong and Hong G. Im

Abstract Theoretical framework and high-fidelity direct numerical simulations (DNS) on preignition and knock encountered in internal combustion (IC) engines are briefly reviewed in this chapter. The theoretical framework is presented first, and systematically followed by one-dimensional and multi-dimensional simulations. A number of high-fidelity simulations under realistic IC-engine conditions were used to demonstrate the super-knock mechanism in the presence of the complex chemistry-turbulence interaction. The ratio of ignition delay time to eddy-turnover time, τ_{ig}/τ_t , and the ratio of the most energetic length scale of turbulence and temperature fluctuations, l_t/l_T , affect the knock intensities are discussed. Different statistical metrics extracted from the multi-dimensional simulations to predict knock intensity are also presented. The quantitative determination of strong and weak ignition modes using the predicted Sa-based metrics is also cover in this chapter.

Keywords Direct numerical simulation (DNS) · Ignition criteria · Strong ignition · Weak ignition

1 Introduction

Modern downsized and boosted internal combustion (IC) engines provide higher thermodynamic efficiencies and cleaner combustion. However, these engines operated under extreme conditions of high load suffer from a higher possibility of abnormal preignition process, a premature auto-ignition induced by hot spots leading to ignition front propagation [1–7]. The mechanism and the source of such irregular preignition events are still not well-understood [8]. The early flames developed from preignition kernels increase the temperature and pressure of the end-gas that may induce a stronger end-gas auto-ignition, leading to extremely high-knock intensities, and even super-knock under high-load and/or high-temperature conditions. As represen-

M. B. Luong (✉) · H. G. Im
Clean Combustion Research Center, King Abdullah University of Science and Technology,
Thuwal, Saudi Arabia
e-mail: minhbau.luong@kaust.edu.sa

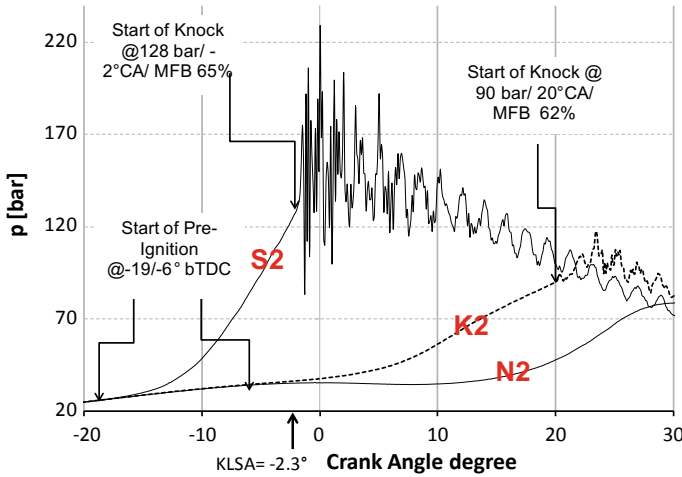


Fig. 1 Examples of in-cylinder pressure traces show preignition and superknock in a turbocharged SI engine: super-knock cycle (S2) with preignition at 19 CAD BTDC and KI \sim 14.5 MPa, moderate knock cycle (K2) with preignition at 6 CAD BTDC and KI \sim 2.4 MPa, and normal (N2) cycle without preignition (taken from Refs. [6, 7])

tatively shown in Fig. 1 [6], super-knock cycle (S2) is characterized by high-pressure amplitudes and intensities due to localized detonation development that may lead to severe structural damage to the engine components. Therefore, a reliable criterion to predict irregular combustion phenomena is of critical importance [1, 3, 4, 6, 9–12].

A large spectrum of turbulence length and time scales combined with extremely short time scales of complex combustion process in detonation simulations pose a significant challenge in reproducing the phenomena using computational simulations, which require extremely fine spatial and temporal resolutions to capture the highly intermittent localized characteristics. This chapter reviews our recent efforts to investigate the fundamental issues of the knock events using high-fidelity direct numerical simulations (DNS) with the capability of fully resolving all temporal and spatial scales and the complex interaction of thermochemistry and turbulence [3, 4, 13, 14]. First-principle DNS is capable of unraveling the complex interplay between turbulence and chemical reactions to provide a better understanding of the mechanism of detonation development encountered in modern combustion devices under extreme high-load operating conditions, and to develop a reliable predictive model for real-world industrial applications [15–31].

In the following, a theoretical framework on super-knock development encountered in internal combustion (IC) engines is briefly reviewed, followed by high-fidelity DNSs in the subsequent sections. A systematically parametric set of two-dimensional (2-D) and three-dimensional (3D) DNS simulations are conducted at engine-relevant conditions [1–4, 32]. Effects of various parameters such as length and time scales of turbulence and scalar fluctuations on the occurrence and intensity of detonation are examined and a scaling relation for knock prediction is proposed [33–43].

2 Developing Detonation Regime Diagram

2.1 Theoretical Background

2.2 Zeldovich's Theory on Reactivity Gradient

According to Zeldovich's theory [44], a spontaneous ignition front is defined as a successive ignition events in the presence of spatial reactivity gradients. Its propagation speed, S_{sp} , is determined as

$$S_{sp} = |\nabla\tau_{ig}|^{-1}, \quad (1)$$

where τ_{ig} is the ignition delay time of the local reactant mixture as schematically shown in Fig. 2, defined as the time to reach the maximum heat release as illustrated in Fig. 3.

Based on the relative ratio of S_{sp} to the laminar flame speed, S_{sp}/S_L , and to the sound speed, S_{sp}/a , of the local mixture as illustrated in Figs. 2 and 3, Zeldovich [44] classified four different ignition regimes of a reaction front propagation in a combustible gaseous mixture:

1. *weak ignition*: In the presence of large spatial variations in τ_{ig} , $S_{sp} \sim S_L$, the local ignition establishes a slow-speed thin-front deflagration (see Figs. 2c and 3).
2. *spontaneous ignition*: For a mixture with a smaller level of τ_{ig} variations, $S_{sp} \gg a$, the mixture ignites spontaneously and S_{sp} exhibits a rapid ignition front propagation (see Figs. 2a and 3).
3. *detonation*: If S_{sp} is sufficiently large and comparable to the sound speed, $S_{sp} \sim a$ as visually shown in Fig. 2b, the combustion wave couple with the acoustic wave may lead to detonation development characterized by extremely high-peak amplitudes of pressure oscillations.
4. *homogeneous ignition*: In the asymptotic limit of zero gradient, S_{sp} becomes infinity, resulting in the purely homogeneous ignition mode.

2.3 $\varepsilon - \xi$ Regime Diagram

Gu and Bradley [45] further mapped different propagation modes into a regime diagram characterized by two key non-dimensional parameters, ξ and ε , which are defined as:

$$\xi = a/S_{sp}, \quad (2)$$

$$\varepsilon = (r_{hs}/a)/\tau_e, \quad (3)$$

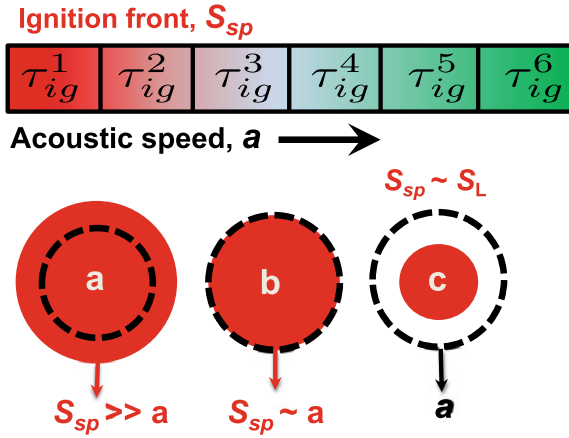


Fig. 2 Schematic of 1-D spatially monotonic distribution of ignition delay times, $\tau_{ig}^1 < \tau_{ig}^2 \dots < \tau_{ig}^6$, (first row), and the relative speed between the reaction front and the acoustic wave (second row) with **a** spontaneous ignition, **b** detonation with a perfect coupling between the reaction front and acoustic wave, and **c** deflagration

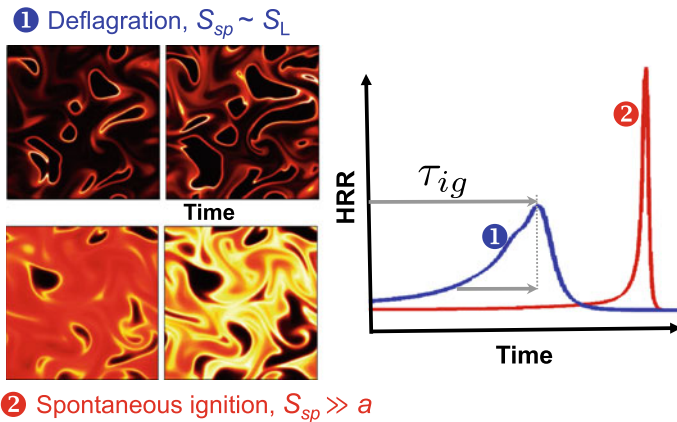
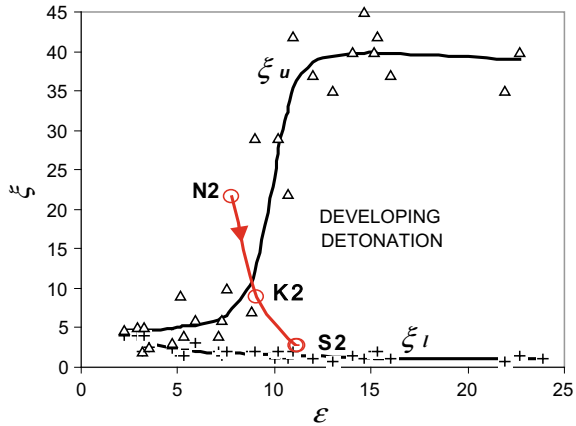


Fig. 3 Representative 2D contours of HRR show deflagrations (first row) and spontaneous ignition fronts (second row) and their temporal evolutions of HRR (right column). The definition of ignition delay time, τ_{ig} , and excitation time, τ_e (the time duration from 5% of the peak HRR to the peak HRR), are shown in the right column

Fig. 4 Conditions for the occurrence of developing detonations in terms of ξ and epsilon for a stoichiometric 50% H_2 -50% CO /air mixture at 5 atm [45, 46]. Three points (S2, K2, and N2) in the red line correspond to the three pressure traces shown in Fig. 1 (taken from Refs. [6, 7])



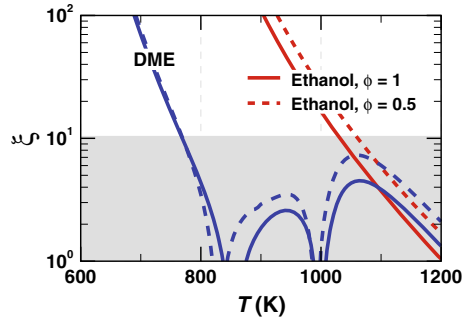
where ε is defined as the ratio of the residence time, r_{hs}/a , of the acoustic wave within the hot spot with a radius, r_{hs} , to the excitation time, τ_e , in which most of the chemical energy is released. τ_e is typically defined as the time interval between 5% of the peak heat release rate (HRR) and the peak HRR as schematically illustrated in Fig. 3.

Based on the range of ξ , five different modes of ignition front propagation within a hot spot were identified [45, 46]:

1. $\xi = 0$ for instant thermal explosion,
2. $0 < \xi < \xi_l$ for spontaneous (supersonic) ignition where the autoignitive wave is ahead of acoustic wave,
3. $\xi_l < \xi < \xi_u$ developing and developed detonation, through the thermoacoustic coupling process referred to as the shock wave amplification by coherent energy release (SWACER) mechanism [47, 48]),
4. $\xi_l \geq \xi < a/S_L$ subsonic autoignitive deflagration where S_L is the laminar burning velocity,
5. $\xi_l \geq \xi < a/S_L$ laminar burning deflagration propagating at the speed comparable to the laminar flame speed.

Figure 4 shows the $\xi - \varepsilon$ peninsula with the upper and lower limit, ξ_u and ξ_l , respectively, between which the developing detonation regime is identified for a stoichiometric 50% H_2 -50% CO /air mixture at 5 atm [45, 46]. Note that the upper and lower ξ limits of the C-shaped curve strongly depend on the initial conditions of T_0 , P_0 , and ϕ_0 , fuel types, and the kinetic model used in simulations [49, 50]. In general, the developing detonation regime is expected when ξ ranges between 1 and $O(10)$ quantity [49, 50]. As representatively shown in Fig. 5, due to the NTC behavior of two-stage ignition fuels (e.g., DME), they are much more prone to detonation development (gray region with roughly $1 < \xi < 10$) than single-stage ignition fuels (e.g., ethanol) for the same initial conditions of temperature, pressure, equivalence ratio, temperature gradient.

Fig. 5 The ξ values as a function of temperature for ethanol/air mixtures (red) and DME/air mixtures (blue) at ϕ of 0.5 and 1.0, and pressure of 35 atm, and $\partial T/\partial r = -2$ K/mm. The shaded region of $1 \leq \xi \leq 10$ is prone to the developing detonation for a small hot spot, i.e., $\varepsilon < 10$



2.4 Quantitative Analysis

Luong et al. [3] proposed three *a posteriori* statistical metrics to quantitatively assess the knock intensity, defined as follows:

$$F_H = \frac{\sum \langle \dot{q} | P > 1.1 P_e \rangle}{\sum \dot{q}}, \tag{4}$$

$$F_{CJ} = \frac{\sum \langle \dot{q} | P > P_{CJ} \rangle}{\sum \dot{q}}, \tag{5}$$

$$F_{VN} = \frac{\sum \langle \dot{q} | P > P_{VN} \rangle}{\sum \dot{q}}, \tag{6}$$

where \dot{q} is the HRR; P_e , P_{CJ} and P_{VN} correspond to the homogeneous constant-volume equilibrium pressure, the Chapman–Jouguet pressure, and the von Neumann pressure, respectively. The summation is operated over all the cells of the computational domain and integrated over time. As such, F_i ($i = e, CJ, VN$) measures the fraction of HRR associated with higher pressures exceeding the corresponding P_i , evaluated at the initial conditions of T_0 , P_0 , and ϕ_0 .

According to Fig. 4 [45], the developing detonation regime is bounded by the upper and lower ξ limits of the C-shaped curve, ξ_u and ξ_l , respectively, suggesting that the detonation intensity depends strongly on the statistical quantities extracted from the spatial distribution of ξ such as its volume-average $\bar{\xi}$, probability density function. To this end, F_D , defined as the volume fraction of $\xi_u < \xi < \xi_l$, is proposed to predict knock intensity:

$$F_D = \int_{\xi_l}^{\xi_u} P(\xi) d\xi, \tag{7}$$

which serves as an *a priori* predictive indicator of the subsequent detonation development while F_H is an *a posteriori* statistical assessment of knock intensity. Note

that both F_D and F_H range from zero to unity. F_D was found to have a strong correlation with the fraction of the total heat release associated with detonation extracted from the full DNS data, F_H [3]. The mixture is found to be more prone to strong detonation as F_D approaches unity if $\varepsilon_p \gtrsim 1$. For each initial condition, F_D together with the volume-average, $\bar{\xi}$, and probability density function, $P(\xi)$, are computed to quantify the knock intensity [3].

In the next sections, the above predictive criteria are discussed using 1D simulations first, followed by selected 2D and 3D simulations with and without turbulence in order to characterize the spontaneous ignition and detonation development.

2.5 One-Dimensional Detonation Development

The developing detonation $\varepsilon - \xi$ diagram [45, 46] has been used in many 1-D studies to investigate the interaction between flame propagation and end-gas auto-ignition, and the effects of boundary conditions, domain size, hot-spot location, hot-spot interaction, and cool flames on subsequent detonation formulation [6, 49–71]. The effects of the bulk-mixture gradient on developing detonation were also studied by Sow et al. [60] and Nogawa and Terashima [72]. In the following, two representative 1-D cases with distinct detonation development characteristics are discussed.

The first case is shown in Fig. 6a features a deflagration to detonation transition (DDT) event where a hot spot is developed into deflagration, gradually consuming the unburned mixture, and finally accelerating to make a transition to detonation. Specifically, the initial temperature profile is designed such that ξ ranges from 0 to 1000 within the hot spot (see Fig. 6). Figure 7 shows the temporal evolution of the temperature and pressure profiles. For such a strong ignition source, autoignition immediately forms a detonation front within the hot spot length, which is subsequently attenuated quickly upon leaving the hot spot (lines 1–4 in Fig. 7). Due to the low reactivity of the unburned mixture at $T_0 = 1000$ K, the heat release rate within the reaction zone is not fast enough to sustain the detonation front such that it decays quickly and transits back into deflagration at $x \sim 10$ mm. As more fuel/air mixture is gradually consumed by deflagration, the temperature and pressure of the remaining unburned mixture ahead of the flame are increased due to the compression heating effect (lines 5–7 in Fig. 7). Due to the increased reactivity of the unburned mixture together with the flame acceleration, the deflagration front transits into detonation at $x \sim 20$ mm and rapidly consumes the rest of the unburned mixture (lines 8–12 in Fig. 7). Much higher pressure peaks are observed during this period. These processes are typically referred as to deflagration to detonation transition (DDT).

The second case (i.e., T_0 of 1200 K with T_{peak} of 1264 K in Fig. 6) features a direct detonation initiation in which the reaction front and the pressure wave are perfectly coupled to form an extremely high shock wave. The initial hot spot is designed for ξ to range between 3 and 6 (see Fig. 6). Due to the high reactivity of the unburned mixture with T_0 of 1200 K, the hot spot immediately gives rise to a detonation front within the hot spot length, thereby rapidly consuming the unburned mixture (see

Fig. 8). Once the detonation is established, the rapid heat release rate in the reaction zone is able to sustain the steady detonation front that propagates and consumes the rest of the unburned mixture.

The above cases show that the two parameters, ξ and ε , within the hot spot and the bulk mixture determines the nature of the early detonation development. Figure 9 shows the compiled results of a series of 1-D simulations for various combinations of these parameters. For a fixed T_0 of 1200 K and ϕ of 1, the 1-D simulations were performed by varying T_{hs} and r_{hs} such that both ξ and ε are varied accordingly. As seen in Fig. 9, the maximum pressure above the equilibrium pressure (i.e., $> 1.1 P_e$) for $0.2 < \xi < 20$. The peak P_{max} occurs at $\xi \sim 6$ where the perfect coupling between the reaction front and the acoustic wave evolving into a stable detonation shock wave. The range of ξ was used to determine the volume fraction of ξ and F_D to predict the amplitude of knock intensity in multi-dimensional cases.

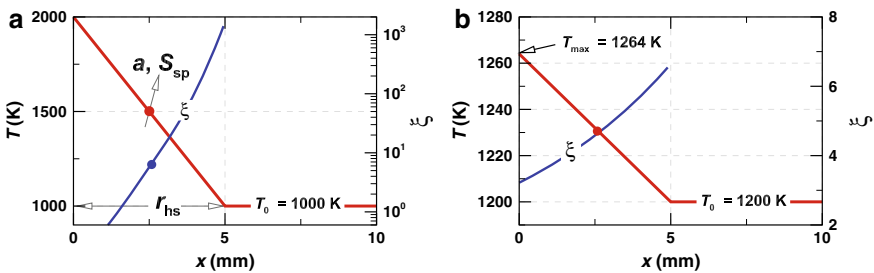


Fig. 6 Two representative initial conditions of a hot spot with a 1-D linear-temperature profile: **a** $T_0 = 1000$ K and $T_{max} = 2000$ K featuring deflagration to detonation transition (DDT) (see Fig. 7), and **b** $T_0 = 1200$ K and $T_{max} = 1264$ K featuring direct detonation development (perfect coupling between the acoustic wave and ignition front, see Fig. 8). The speed of sound, a , and ξ are evaluated at the center of hot spots (marked as dots). The spatial distribution of ξ within the hot spots is also shown. Note that τ_{ig} and τ_e are computed by using a 0-D homogeneous adiabatic constant-volume reactor using the localized temperature and pressure

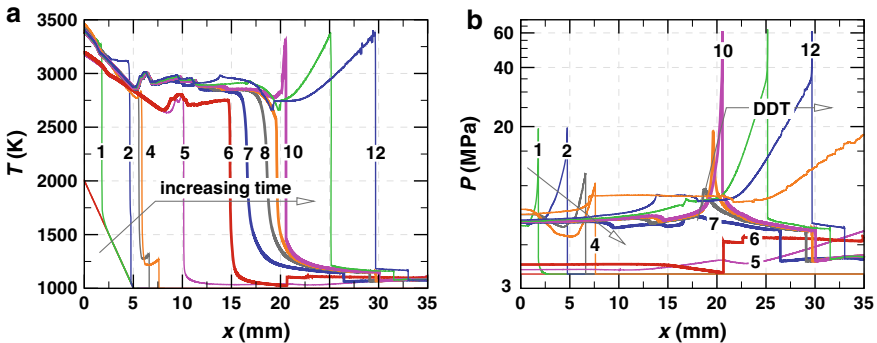


Fig. 7 The temporal evolutions of **a** temperature and **b** pressure at different time. The initial conditions of T_0 of 1000 K and P_0 of 35 atm (see Fig. 6), a stoichiometric ethanol/air mixture

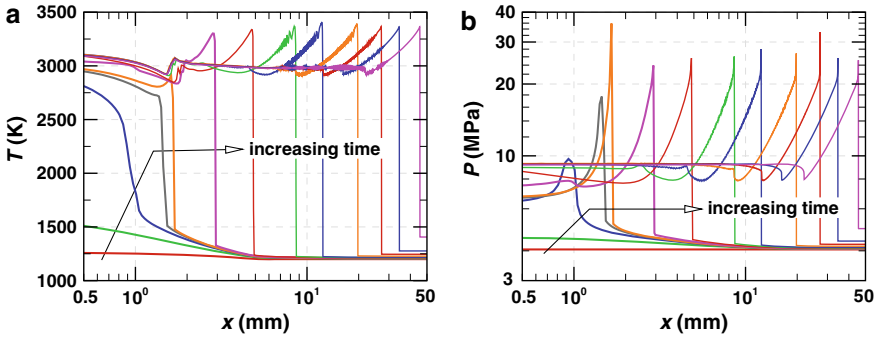


Fig. 8 The temporal evolutions of **a** temperature and **b** pressure at different time. The initial conditions of T_0 of 1000 K and P_0 of 35 atm (see Fig. 6), a stoichiometric ethanol/air mixture

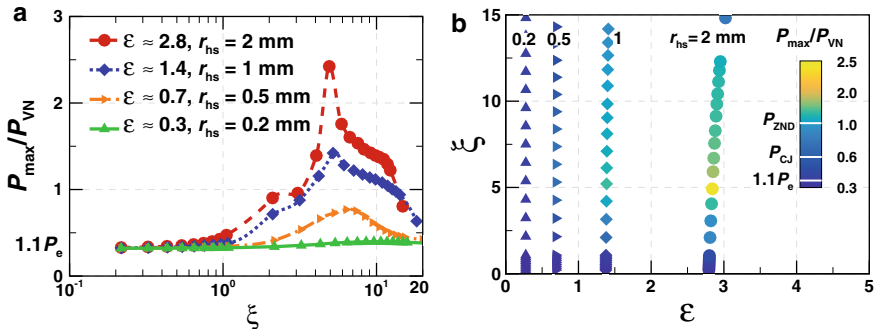


Fig. 9 **a** The normalized maximum pressure as a function of ξ , and **b** the $\xi - \epsilon$ diagram for different hot spot sizes (taken from Luong et al. [3])

2.6 2-D and 3-D Simulations of Super-Knock Under Realistic IC-engine Conditions

The basic characterization in 1D problem is now extended to multi-dimensional conditions in the presence of spatial fluctuations in temperature and velocity fields. Parametric 2-D and 3-D simulations were systematically performed to validate the criteria proposed in Fig. 2.4. The distribution of ξ and ϵ were varied by changing T' over a wide range from 0.5 to 20 K, and l_T of 1, 2, 5, and 10 mm. For each initial condition, the full detailed information of spatial distribution of ξ and the corresponding statistical quantities of ξ can be computed. Figure 10 shows the spatial distribution of ξ of four cases with different T' and l_T that result in no-knock, mild-knock and super-knock [3].

Figure 11 shows a representative 2-D contour of temperature field with T_0 of 1200 K, T' of 15 K, and l_T of 5 mm. According to Peters et al. [53, 73], the temperature field is subdivided into the *dissipation elements* over which the temperature profile

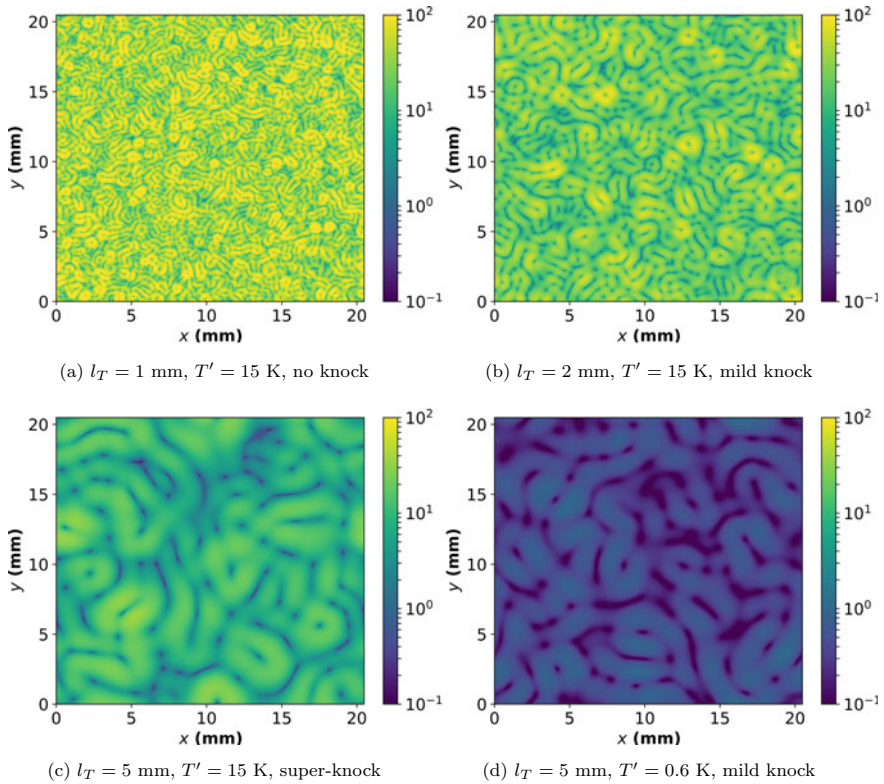
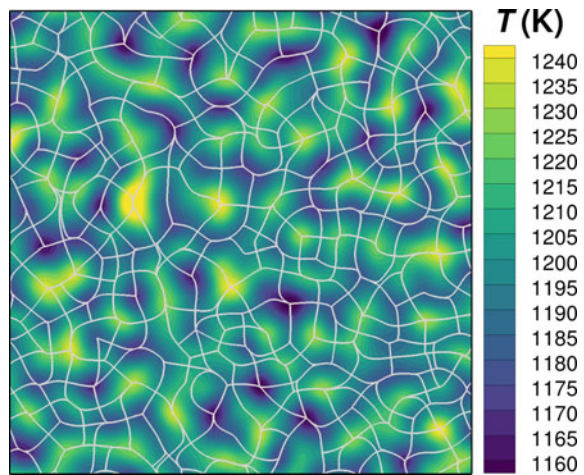


Fig. 10 Representative 2-D contours of ξ distribution computed from four different initial conditions for three different l_T of 1 mm, 2 mm, 5 mm, with T' of 15 K (a-c) and 0.6 K (d)

Fig. 11 Representative 2-D contour of temperature field with T_0 of 1200 K, T' of 15 K, and l_T of 5 mm overlaid by the dissipation elements. The white lines mark the boundary between the dissipation elements



is monotonic, ranging from the peak to the trough of each dissipation element. For isotropic temperature field fluctuations, Peters et al. [53] found r_{hs} comparable with the mean distance of the dissipation elements, l_{DE} , and approximated as $l_{\text{DE}} \approx 2\lambda_T$, where λ_T is the Taylor mixing scale [53]. In the multi-dimensional problems, l_{DE} is believed to be a minimum size of a hot spot of unburned reactants required so that it allows a sufficient run-up distance of detonation development [12, 53].

Based on the Taylor mixing scale, Towery et al. [12] proposed a statistical model to evaluate the predictive ε_p for highly compressible homogeneous isotropic turbulence fluctuations. ε_p is defined as

$$\varepsilon_p = 2\lambda_T / (a_{\text{rms}} \tau_{\text{exo}}) \quad (8)$$

where a and τ_{exo} are the mass-weighted sound speed and exothermicity time, respectively (see Ref. [12] for details). In Refs. [3, 4], at the the initial conditions of $T_0 = 1200$ K, $P_0 = 35$ K, and $\phi_0 = 1$, $\varepsilon_p = 1$ corresponds to the initial temperature field of $l_T = 3.3$ mm. The cases with $\varepsilon_p < 1$ (i.e., l_T of 1 and 2 mm with ε_p of 0.3 and 0.6) are less likely to develop detonation while the cases with ε_p of 1.2, 1.4, and 3.8 for l_T of 4 mm, 5 mm, and 10 mm, respectively, are more likely to develop strong detonation if $1 < \xi < 10$.

For a uniform mixture with only thermal fluctuations, the predictive ξ_p is scaled as [11, 12]

$$\xi_p = a \left| \frac{d\tau_{\text{ig}}}{dT} \nabla T \right| \cong a \left| \frac{d\tau_{\text{ig}}}{dT} \right| |\widetilde{\nabla T}| \quad (9)$$

where the statistical mean temperature gradient is further approximated by $|\widetilde{\nabla T}| \cong T' / \lambda_T$, with the Taylor mixing length scale, $\lambda_T \cong (l_T \alpha / T')^{0.5}$ [11]. These predictive parameters, ξ_p , and ε_p , will be validated in the subsequent sections.

2.6.1 Baseline Cases with No Turbulence

In this subsection, three baseline (no turbulence) cases with l_T of 1 mm, 2 mm, and 5 mm denoted as BL1, BL2, and BL5, respectively, are chosen for discussion. The probability density functions (PDF) of ξ , the temporal evolution of the normalized P_{max} , and the contours of pressure at the time of the peak of F_H for three baseline cases are shown in Figs. 12 and 13. According to the scaling of ξ_p above, with a fixed T' of 15 K, increasing l_T from 1 to 5 mm decreases ξ_p which is consistent with the PDF of ξ shifting toward the developing detonation regime (see Fig. 12). Consequently, BL5 is predicted to be more prone to developing detonation as compared to BL1 and BL2.

Consistent with the PDFs of ξ and $\varepsilon_p = 0.3$, $P_{\text{max}} \leq P_{\text{VN}}$ and the isocontours of pressure in Figs. 12 and 13, respectively, confirm that BL1 features a spontaneous ignition process. BL2 with $F_{\text{VN}} \approx 0.07$ is characterized as a mild detonation process as also quantitatively predicted by $\varepsilon_p = 0.6$. Unlike BL1 and BL2, a strong detonation

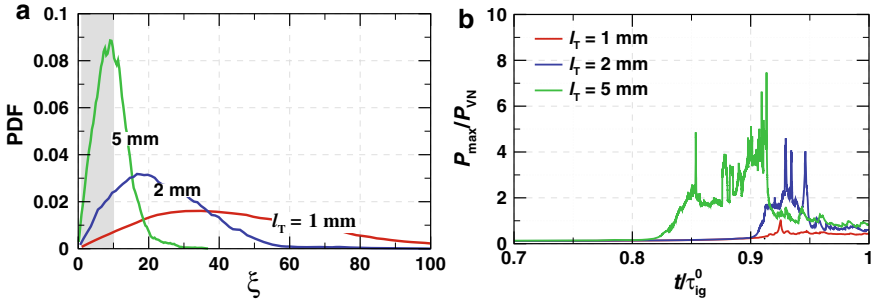


Fig. 12 **a** The probability density functions (PDF) of ξ for three baseline cases (without turbulence) with three different most energetic length scale of temperature, l_T of 1 mm, 2 mm, and 5 mm, featuring no knock, mild knock, and super-knock, respectively, and **b** their temporal evolution of the normalized maximum pressure, P_{\max}/P_{VN} . [4]. The gray area in the PDF figure depicts the region of $1 < \xi < 10$ determined by a series of 1-D simulations under the same initial conditions, which is prone to developing detonation (see Fig. 9a) (adapted from Luong et al. [3, 4])

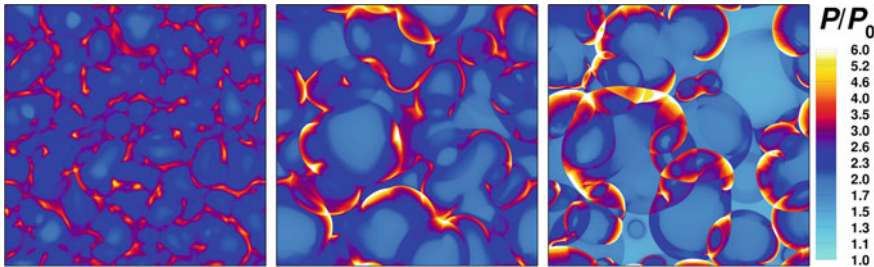


Fig. 13 Representative 2-D contours of pressure for three cases with the same T' of 15 K, and l_T of 1 mm, 2 mm, and 5 mm with no knock, mild knock, and super-knock, from left to right, respectively (adapted from Luong et al. [3])

process is observed for BL5, quantified by $F_{VN} \approx 0.2$ and $P_{\max} \gg P_{VN}$, which is accurately predicted by $\varepsilon_p = 1.6$ for BL5.

The statistical quantities, F_H , F_D and $\bar{\xi}$, of all the baseline cases are plotted in Fig. 14. Three main points are noted from Fig. 14. First, F_D has a better agreement with F_H for $\varepsilon_p > 1$ (i.e., cases with $l_T > 4$ mm in Fig. 14b). Second, the magnitude of F_H for 3-D cases is comparable with the corresponding 2-D cases as seen in Fig. 14a despite the peak F_{VN} of the 3-D cases slightly lower than that of the 2-D cases [3]. Third, Fig. 14 also reveals a good correlation between $\bar{\xi}$ and the knock intensity characterized by the F_H magnitude. The correlation indicates that the conditions with $\bar{\xi}$ ranging between 0.5 and 30 experience developing detonation and the strongest detonation intensity (F_H approaches unity) occurs at $\bar{\xi} \sim 6$ with $\varepsilon_p > 1$. Specifically, the maximum values of F_H at $\bar{\xi} \sim 6$ are approximately 0.18, 0.22, 0.55, and 0.75 for l_T of 1 mm, 2 mm, 5 mm, and 10 mm, respectively. These results verify that the prediction of ε_p for knock propensity is consistent with F_H , the detonation intensity is greatly alleviated with decreasing l_T (mild-to-no detonation for $l_T < 3.3$ mm with $\varepsilon_p < 1$).

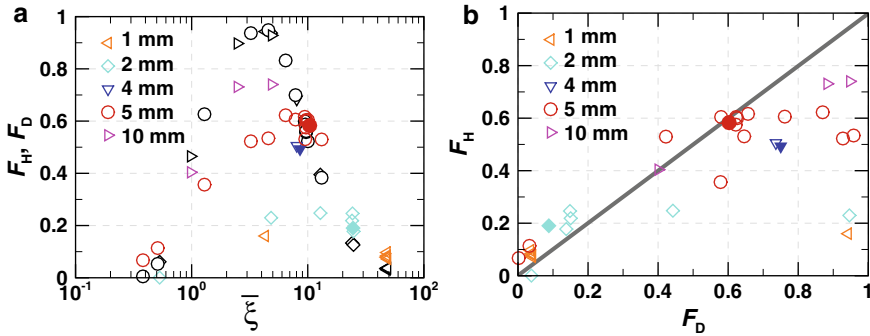


Fig. 14 **a** F_H (color symbols) and F_D (black symbols) as a function of $\bar{\xi}$, with T' ranging from 0.5 K to 20 K for different l_T ranging from 1 mm to 10 mm, **b** the correlation between F_H and F_D . Filled (open) symbols are for 3-D (2-D) cases (taken from Luong et al. [3])

2.6.2 Effect of Turbulence

The previous subsection demonstrated that no detonation was observed for BL1 while BL5 exhibited a strong detonation process because a minimum run-up distance is required for developing detonation as accurately predicted by ε_t . The results suggest that decreasing (increasing) the length scale of temperature fluctuations (hence the dissipation element length) is a key parameter to alleviate (promote) knock intensity. In this subsection, the additional effect of turbulent velocity fields on knock intensity is also investigated [4].

The isocontours of pressure and HRR of two representative 2-D simulations and a 3-D simulation in Figs. 15, 16 and 17 are chosen for discussion. With the same turbulent velocity fluctuation, u' of 83.3 m/s, and root-mean-square temperature fluctuation, T' of 15 K, l_T/l_e and τ_{ig}/τ_t were found to be two key parameters to determine knock propensity.

First, increasing turbulent intensity by increasing u' and fixing $l_e = 5$ mm is not effective in reducing knock intensity since with τ_{ig}/τ_t of 1.0, turbulence is not fast enough to modify the autoignition and the subsequent detonation process as visually seen in Fig. 16. Rather, the main effect of turbulent eddies is to weakly wrinkle and distort the detonation fronts. Second, a finer turbulence structure, l_e of 1 mm $\ll l_T = 5$ mm, and τ_{ig}/τ_t of 5.0, effectively attenuates the detonation intensity as visually seen in Figs. 16 and 17. High turbulence intensity together with a short mixing-time scale significantly increases the amount of reactants burned by corrugating turbulent flames rather than by the developing detonation phase. Fast and small turbulence structures also induce smaller and finer localized detonation waves during the developing detonation process. Third, for the 3-D cases with a slightly lower F_H , a consistent agreement between the 2-D and 3-D cases was observed in terms of P_{max} , the duration of detonation process, and the level of pressure oscillations, P' [4].

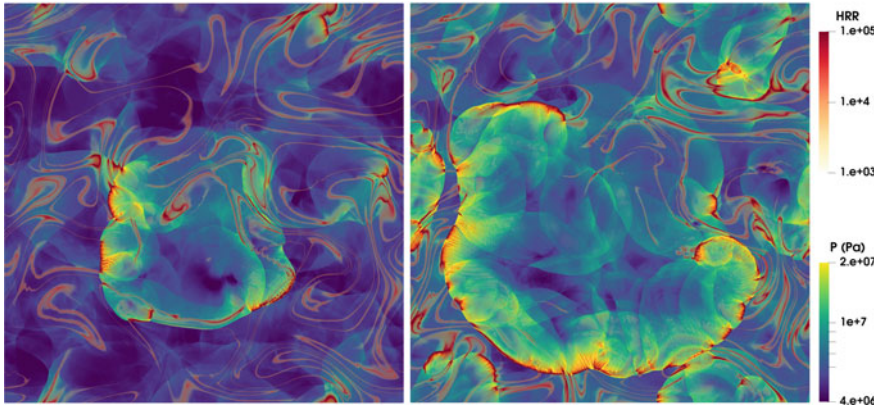


Fig. 15 Two-dimensional contours of pressure and heat release rate (HRR) at the times of onset of detonation development (left) and the peak detonation intensity (right) for a 2-D case with the most energetic length scale of temperature and turbulent field, l_T of 5 mm and l_e of 5 mm, respectively, the turbulent velocity fluctuation, u' of 83.3 m/s, and the ratio of the ignition delay time to turbulent time scale τ_{ig}/τ_t of 1.0 [4] (taken from Desai et al. [14])

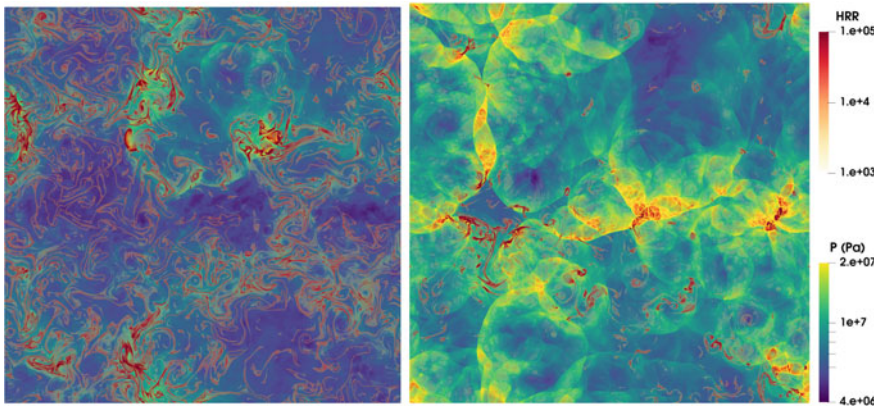


Fig. 16 Two-dimensional contours of pressure and heat release rate (HRR) at the times of onset of detonation development (left) and the peak detonation intensity (right) for a 2-D case with the most energetic length scale of temperature and turbulent field, l_T of 5 mm and l_e of 1 mm, respectively, the turbulent velocity fluctuation, u' of 83.3 m/s, and the ratio of the ignition delay time to turbulent time scale τ_{ig}/τ_t of 5.0 [4] (taken from Desai et al. [14])

Contrary to the case with $l_e = 1 \text{ mm} \ll l_T = 5 \text{ mm}$ being able to attenuate detonation intensity, a fast turbulent mixing, τ_{ig}/τ_t of 5, together with $l_e = 5 \text{ mm} \gg l_T = 1 \text{ mm}$, promotes detonation development as seen in Fig. 18. Turbulence with a larger eddy size effectively spreads the temperature field over a wider area, stretching out the run-up distance, and thus facilitates the developing detonation [4].

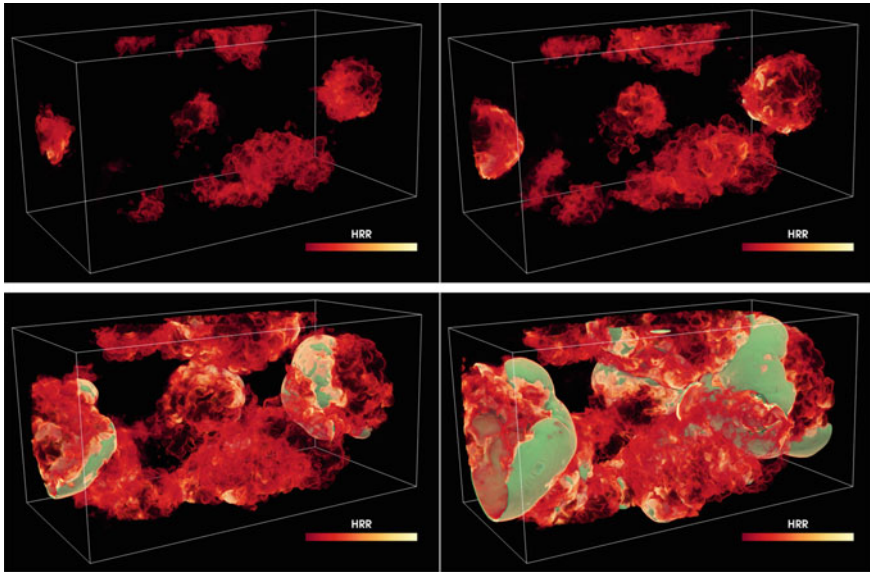
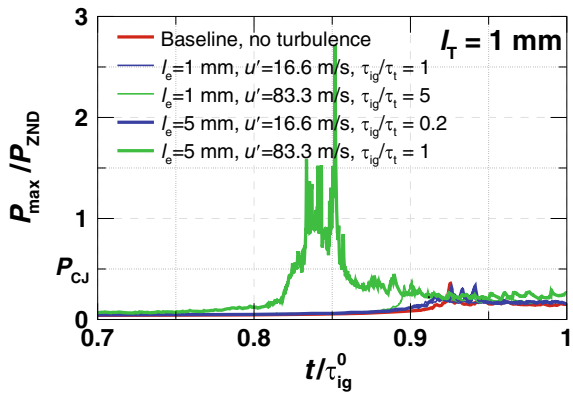


Fig. 17 The volume rendering of HRR and the iso-surface of pressure (green) with $P = P_{CJ}$ at successive times prior to the onset of the detonation formation (top row) until the detonation intensity reaches its peak (bottom row) for a 3-D case with the most energetic length scale of temperature and turbulent field, l_T of 5 mm and l_e of 1 mm, respectively, the turbulent velocity fluctuation, u' of 83.3 m/s, and the ratio of the ignition delay time to turbulent time scale τ_{ig}/τ_t of 5.0 [4] (taken from Desai et al. [14])

Fig. 18 Temporal evolution of the normalized maximum pressure, P_{max}/P_{VND} for the cases with l_T of 1 mm with different l_e and u' (adapted from Luong et al. [4])



3 Weak and Strong Ignition Modes

3.1 Theoretical Background

Based on Zeldovich’s theory and validated by high-fidelity DNS data, Sankaran et al. [15] proposed a criterion to delineate the weak or strong ignition modes, referred to as the Sankaran number (Sa) herein, which is based on the ratio of laminar flame speed, S_L , to the ignition front speed, $S_{sp} = |\nabla\tau_{ig}|^{-1}$ [44].

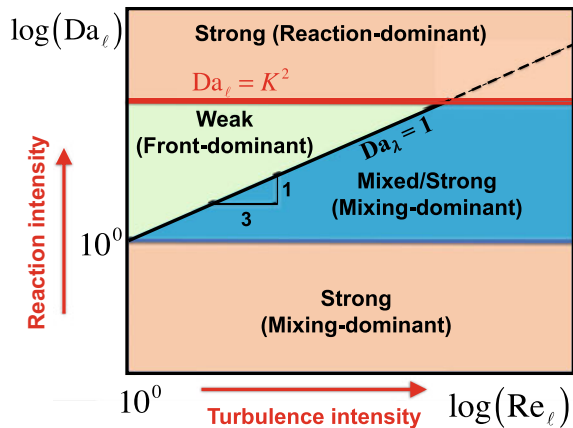
$$Sa = \beta \frac{S_L}{S_{sp}}, \tag{10}$$

where β is a weighting factor of 0.5 to account for some delay in developing a deflagration from the ignition kernel due to the interactions of thermal and radial diffusion between the neighboring regions. $Sa = 1$ serves as the boundary between the strong ($Sa < 1$) and the weak ($Sa > 1$) ignition.

In practical combustion devices, the detailed information of the spatially resolved scalar fluctuations is not available, and thus the prediction for in a real engine should be based on the statistical quantities such as the mean and variance of fluctuations in RANS or LES simulations. Im et al. [11] conducted a theoretical scaling analysis by incorporating the turbulent effect into the original Sankaran criterion to derive the turbulent ignition regime diagram as shown in Fig. 19.

For compositionally homogeneous reactant mixtures with turbulent velocity and temperature fluctuations, the diagram classifies ignition modes into three categories: *weak* exhibiting a dominant slow-speed deflagration mode of fuel consumption, *reaction-dominant strong*, and *mixing-dominant strong* exhibiting a dominant volumetric-ignition mode of fuel consumption. Pal et al. [74] and Luong et al. [1] conducted a series of DNS simulations and found consistent results with the pre-

Fig. 19 Regime diagram proposed by Im et al. [11] for strong and weak ignition modes for nearly homogeneous reactant mixture with velocity and temperature fluctuations



dictions by the turbulent ignition regime diagram. The ignition criterion [11] was further extended to accommodate both temperature and concentration fluctuations and validated for the mixtures with NTC and non-NTC behaviors [1].

The gradient of ignition delay time, $\nabla\tau_{\text{ig}}$, for a mixture with a uniform composition and pressure is solely due to temperature variations expanded by the chain rule as [11]:

$$|\nabla\tau_{\text{ig}}| = \left| \frac{d\tau_{\text{ig}}}{dT} \nabla T \right|, \quad (11)$$

where $d\tau_{\text{ig}}/dT$ represents the ignition delay sensitivity to temperature as representatively shown in Fig. 20b, and ∇T is the temperature gradient of the bulk mixture [11, 74]. In turbulent conditions, the temperature gradient is approximated by the statistical mean temperature gradient, $|\widetilde{\nabla T}|$, which is estimated based on the variance of the temperature, T' , fluctuations and the Taylor mixing scale, λ_T , as

$$|\widetilde{\nabla T}| \approx \frac{T'}{\lambda_T}, \quad (12)$$

where the Taylor mixing scale is approximated as

$$\lambda_T = l \text{Re}_l^{-0.5}, \quad (13)$$

with $\text{Re}_l = u'l/\nu$ being the turbulent Reynolds number, ν the kinematic viscosity of the bulk mixture gas, u' the root mean square (RMS) turbulent velocity fluctuation, and l the integral scale of velocity field.

Further scaling analysis yields the expression for the *predicted* Sankaran number, Sa_p , [11] as follows:

$$\text{Sa}_p = K \text{Da}_l^{-1/2}, \quad K = \beta \frac{1}{(\tau_f \tau_{\text{ig}})^{1/2}} \left| \frac{d\tau_{\text{ig}}}{dT} T' \right|, \quad (14)$$

where $\text{Da}_l = \tau_i/\tau_{\text{ig}}$ is the ignition Damköhler number, defined as the ratio of the turbulence integral time scale, l/u' , to the ignition delay time, and $\tau_f = \alpha/S_L^2$ is the characteristic flame time, where α is the thermal diffusivity of the initial bulk mixture. K is referred to as the normalized thermal ignition sensitivity.

In the presence of both temperature and equivalence ratio (concentration) fluctuations, τ_{ig} is a function of T and ϕ such that $|\nabla\tau_{\text{ig}}|$ is expanded by using the chain rule as flows:

$$|\nabla\tau_{\text{ig}}| = \left| \frac{\partial\tau_{\text{ig}}}{\partial T} \nabla T + \frac{\partial\tau_{\text{ig}}}{\partial\phi} \nabla\phi \right|, \quad (15)$$

where $\nabla\phi$ and $\partial\tau_{\text{ig}}/\partial\phi$ are the equivalence ratio gradients, and the ignition delay sensitivity to equivalence ratio, respectively [1]. Assuming that the temperature and equivalence ratio fields are correlated with the turbulent flow field, it results in a

comparable integral length scale, $l_T \sim l_\phi \sim l_e$, and $\widetilde{\nabla\phi} \sim \phi'/\lambda_T$ as approximated in the temperature case.

As such K in Fig. 14 is extended as:

$$K = \beta \frac{1}{(\tau_f \tau_{ig})^{1/2}} \left(\left| \frac{\partial \tau_{ig}}{\partial T} T' \right| + s \left| \frac{\partial \tau_{ig}}{\partial \phi} \phi' \right| \right), \quad (16)$$

where the sign of s is to account for the NTC behavior and the correlation of T - ϕ distribution. s is positive if T and ϕ fluctuations are uncorrelated, thereby being additive to $|\nabla \tau_{ig}|$ that synergistically promotes the deflagration mode regardless of the NTC regime. s adopts a negative (positive) sign for a negative $T - \phi$ correlation if the product of $\partial \tau_{ig}/\partial T$ and $\partial \tau_{ig}/\partial \phi$ is positive (negative) that the combined effects of T and ϕ on K become subtractive (additive).

3.2 Prediction of Weak/strong Combustion Modes

Many fuels with and without the NTC behavior were chosen to investigate the effect of temperature and equivalence ratio fluctuations on the combustion modes by varying the initial mean temperatures and different fluctuation levels [1, 20, 27, 28, 30, 75–77]. The initial conditions and physical parameters are chosen to be relevant to IC engine conditions [1, 33–43]. The DNS solution were processed to verify the predictive accuracy of the ignition criteria.

Figure 20 shows the homogeneous ignition delay time of DME/air mixtures and ethanol/air mixtures and the sensitivity of ignition delay time to temperature that is needed to compute Sa_p . DME exhibits the negative-temperature coefficient (NTC) regime in which τ_{ig} increases with increasing temperature such that its τ_{ig} varies non-monotonically with temperature. As such, within/near the NTC regime, the variation of $d\tau_{ig}/dT$ for DME is small compared to that of single-stage fuels (e.g., ethanol), which in turn leads to a small $|\nabla \tau_{ig}|$ for the same temperature fluctuation level. It suggests that within/near the NTC regime, the mixture with T' only is more susceptible to spontaneous ignition as quantitatively predicted by Sa_p in Fig. 21 [2].

Figure 22 shows a typical initial condition used in the simulations. These DNS cases were adopted to perform the statistical analysis of Sa such that the volume-average (mean) Sa , \bar{Sa} , the probability density function of Sa , $P(Sa)$, and the volume fraction of the regions with $Sa < 1$, $F_{Sa,S}$, extracted from the spatial Sa distribution are obtained. In addition, Sa_p for each simulation was also computed based on the information of the initial mean bulk mixture condition such as T_0 , p_0 , and ϕ_0 , and the RMS values, T' and ϕ' as representatively shown in Fig. 21 as a function of temperature.

The isocontours of HRR for some representative DME cases are shown in Fig. 23. Spontaneous ignition characterized by volumetric ignition is dominant even with T' of 60 K at T_0 of 900 K due to a small variation of τ_{ig} with temperature within/near the

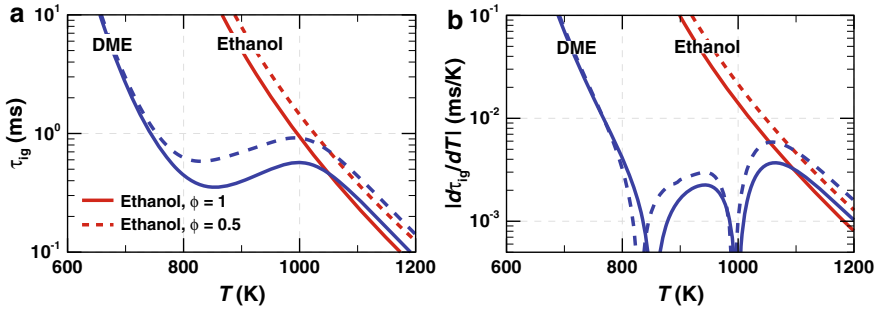
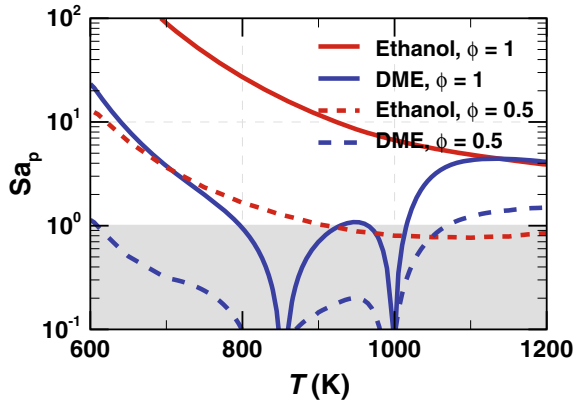


Fig. 20 **a** The 0-D homogeneous ignition delay time, τ_{ig} , and **b** the absolute value of the sensitivity of τ_{ig} to temperature, $|d\tau_{ig}/dT|$, as a function of temperature for ethanol/air mixtures (red) and DME/air mixtures (blue) at ϕ of 0.5 and 1.0, and pressure of 35 atm

Fig. 21 The predicted Sa number, Sa_p , as a function of temperature for ethanol/air mixtures (red) and DME/air mixtures (blue) at ϕ of 0.5 and 1.0, and pressure of 35 atm, and assuming the identical integral length scale of velocities and temperature field, $l_t = l_T = 1$ mm, $\tau_t/\tau_{ig} = 1$, and $T' = 15$ K. The shaded region of $Sa_p < 1$ is for strong ignition, while the region of $Sa_p > 1$ is for weak ignition



NTC regime as shown in Fig. 20). On the contrary, deflagration propagation becomes dominant for the cases with T_0 of 680 and 1045 K outside the NTC regime. Similar results were found for *n*-heptane [20, 29–31, 75, 76, 78, 79].

Contrary to the T' -only cases, in the presence of both T and ϕ , especially when they are negatively correlated, T_0 of 900 K results in a much lower HRR (due to the synergistic effect of T' and ϕ') than those of T_0 outside the NTC regime (due to the subtractive effect of T' and ϕ' for the cases with T_0 of 770 and 1045 K), as seen in the bottom row of Fig. 23.

Quantitative assessment of combustion modes for the previous cases was also conducted. For each initial field of a DNS case, the exact distribution of Sa within the domain and its associated statistical quantities can be computed. For direct validations with the predictive quantities such as F_5 and $\bar{S}a$, the fractional contributions of weak and strong ignition to the total heat release were extracted from the detailed DNS solution.

Figure 22a-b shows representative initial fields of temperature and equivalence ratio distribution. Based on these detailed DNS information, the spatial distribution

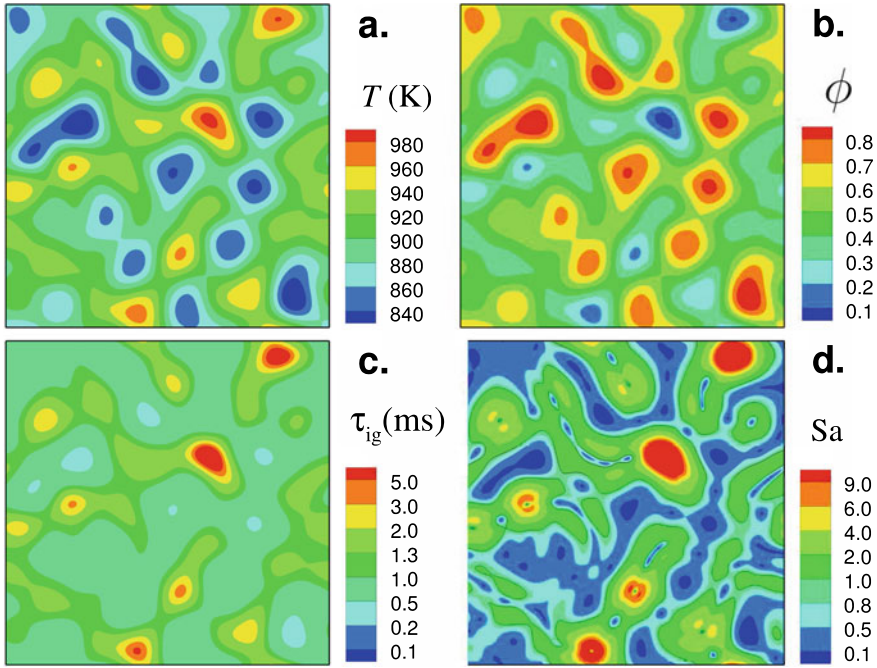


Fig. 22 a–b initial fields of temperature and equivalence ratio with a negative $T-\phi$ distribution at the initial mean temperature and equivalence ratio of 900K–0.5 with their fluctuation of T' and ϕ' of 30K and 0.15, respectively, and c–d the corresponding ignition delay time and Sa distribution. The black iso-lines of $Sa = 1$ delineates two distinct combustion modes of strong ($Sa < 1$) and weak ($Sa > 1$) ignition (taken from Luong et al. [2])

of τ_{ig} and Sa , and the corresponding probability density function (PDF) of Sa , $P(Sa)$ are computed in Figs. 22c–d and 24, respectively. The volume fraction of the regions attributed to strong ignition was also estimated as

$$F_{Sa,S} = \int_0^1 P(Sa)dSa, \tag{17}$$

which was proposed as a quantitative metric to predict the fractional cumulative heat release rate associated with strong ignition directly computed from DNS solution fields, $F_{Da,S}$ as [20, 27, 28, 30, 75, 76]

$$F_{Da,S} = \frac{\sum \langle \dot{q} | Da > Da_0 \rangle}{\sum \dot{q}}, \tag{18}$$

where the summation is operated over the total number of computational cells in the DNS domain, \dot{q} is the HRR, and Da is Damköhler number defined as the ratio of the

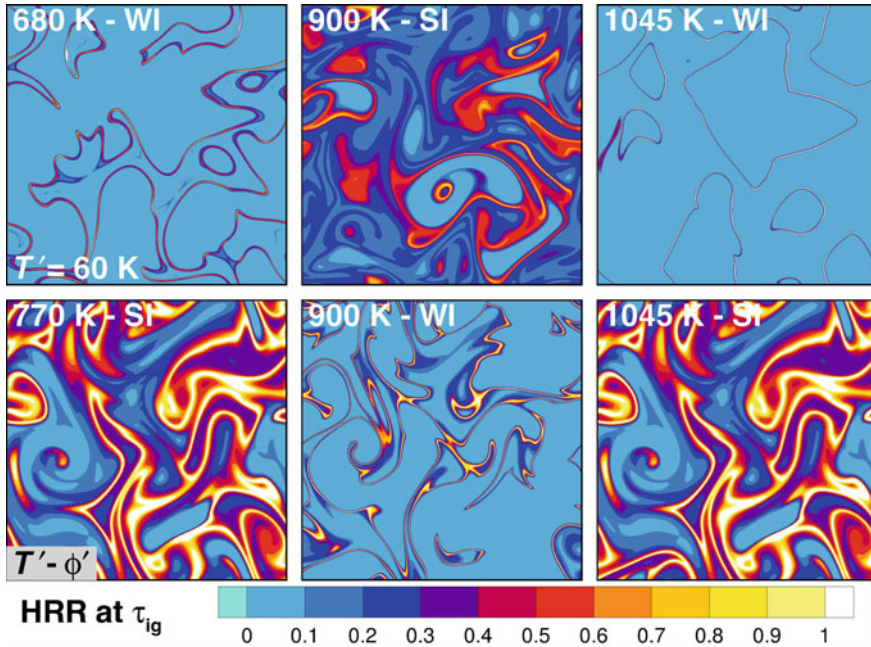


Fig. 23 2-D contours of the normalized HRR at the maximum spatial-averaged HRR occurrence for the DME/air mixtures at the initial pressure of 30 atm. The first (second) row corresponds to the cases with temperature fluctuations only, T' of 60 K, (with both temperature and equivalence ratio fluctuations, T' of 30 K and ϕ' of 0.15 [2]) (adapted from Luong et al. [1])

local reaction and diffusion terms for a selected scalar variable [16, 17, 20, 28, 30, 71, 75, 76, 80]. Strong ignition is dominant if $F_{Sa,S} \sim 1$. Strong and weak ignition is delineated by a threshold value, Da_0 , of order unity that depends on the chosen initial condition. The significance of the Sa-based metric is that the prediction of combustion modes is based purely on the initial conditions.

Consistent with the qualitative observations in the previous section, \bar{Sa} and $F_{Sa,S}$ for the DME cases of T_0 at 680 K, 900 K, and 1045 K are found to be, respectively, 4.2 & 0.20, 0.5 & 0.92, and 1.3 & 0.4. The cases with T_0 of 680 K and 1045 K have \bar{Sa} greater than one, suggesting a weak-ignition dominance, while for the case with T_0 of 900 K, a strong ignition is expected. The predictive accuracy of \bar{Sa} and $F_{Sa,S}$ is further verified by the magnitude of $F_{Da,S}$ as shown in Fig. 25.

Figure 25 shows a strong correlation between $\bar{Sa}_n = \bar{Sa}/(1 + \bar{Sa})$ and $F_{Sa,S}$ regardless of T_0 , T' , ϕ' , and fuel types. A good correlation between Sa_p and $F_{Sa,S}$ was also demonstrated, which is attributed to the agreement between the predicted Sa_p and the volume-average \bar{Sa} . Based on this universal correlation, the magnitude of either \bar{Sa} or Sa_p can be used to quantitatively infer $F_{Sa,S}$, which characterize the combustion intensity. In general, a higher \bar{Sa} corresponds to a lower $F_{Sa,S}$, which translates into a lower combustion intensity. In particular, $\bar{Sa}_n = 0.5$ serves as a transition point from

Fig. 24 A representative probability density function of Sa distribution, PDF(Sa). SI and WI denote strong ignition and weak ignition, respectively with a threshold of Sa = 1 (taken from Luong et al. [2])

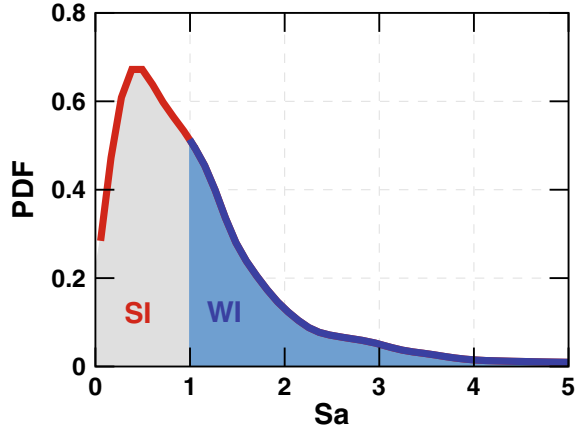
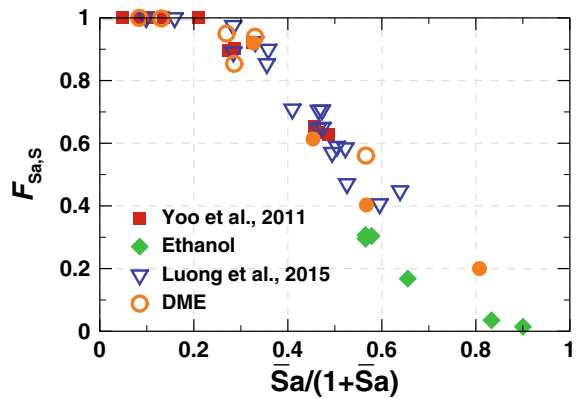


Fig. 25 The volumetric fraction of Sa < 1, $F_{Sa,S}$, as a function of the normalized Sa, $\bar{Sa}_n = \bar{Sa}/(1+\bar{Sa})$ to fit within a range between 0 and 1, with 0.5 corresponding to Sa = 1 (taken from Luong et al. [1])



SI to WI dominance with 60% heat released by spontaneous ignition mode ($F_{Sa,S} = 0.6$). Spontaneous ignition dominance ($F_{Sa,S} = 1.0$) occurs at $\bar{Sa} < 0.3$. On the contrary, weak ignition is expected to be dominant at $\bar{Sa} > 1.0$. In summary, either \bar{Sa} or Sa_p can be used to quantitatively predict the combustion modes over a wide range of initial conditions and different fuel types.

4 Summary

Recent developments in the theoretical study to predict detonation development in IC engine conditions were summarized. A brief review was given on the theoretical framework, starting from the original Zeldovich theory, and the regime diagrams per Bradley [46] and Im [11], and various proposed predictive criteria by Luong et al. [3, 4]. A large collection of DNS simulation data were used for *a priori* and *a posteriori*

test for the validation of different predictive criteria based on the initial solution field, and its extension to large turbulent conditions with statistical average and variances has been suggested.

In real combustion engines, additional complexities arise from the front-to-wall and front-to-front interactions which may further enhance or suppress the occurrence and intensity of the detonation event. This is of strong practical significance and is currently being investigated by large-scale simulations [3, 4].

Acknowledgements This work was sponsored by King Abdullah University of Science and Technology and used the resources of the KAUST Supercomputing Laboratory.

References

1. Luong MB, Hernández Pérez FE, Im HG (2020) Prediction of ignition modes of NTC-fuel/air mixtures with temperature and concentration fluctuations. *Combust Flame* 213:382–393
2. Luong MB, Hernández Pérez FE, Sow A, Im HG (2019) Prediction of ignition regimes in DME/air mixtures with temperature and concentration fluctuations. *AIAA SciTech 2019 Forum* <https://doi.org/10.2514/6.2019-2241>
3. Luong MB, Desai S, Hernández Pérez FE, Sankaran R, Johansson B, Im HG (2020) A statistical analysis of developing knock intensity in a mixture with temperature inhomogeneities. *Proc Combust Inst* 37
4. Luong MB, Desai S, Hernández Pérez FE, Sankaran R, Johansson B, Im HG (2006) Effects of turbulence and temperature fluctuations on knock development in an ethanol/air mixture. *Flow Turbul Combust*
5. Wang Z, Liu H, Reitz RD (2017) Knocking combustion in spark-ignition engines. *Prog Energy Combust Sci* 61:78–112
6. Kalghatgi GT, Bradley D (2012) Pre-ignition and ‘super-knock’ in turbo-charged spark-ignition engines. *Int J Engine Res* 13:399–414
7. Kalghatgi GT (2015) Developments in internal combustion engines and implications for combustion science and future transport fuels. *Proc Combust Inst* 35:101–115
8. Figueroa-Labastida M, Badra J, Elbaz AM, Farooq A (2018) Shock tube studies of ethanol preignition. *Combust. Flame* 198:176–185
9. Meyer JW, Oppenheim AK (1971) On the shock-induced ignition of explosive gases. *Symp (Int) Combust* 13:1153–1164
10. Lutz AE, Kee RJ, Miller JA, Dwyer HA, Oppenheim AK (1989) Dynamic effects of autoignition centers for hydrogen and c1, 2-hydrocarbon fuels. *Symp (Int) Combust* 22:1683–1693
11. Im HG, Pal P, Wooldridge MS, Mansfield AB (2015) A regime diagram for autoignition of homogeneous reactant mixtures with turbulent velocity and temperature fluctuations. *Combust Sci Technol* 187:1263–1275
12. Towery CAZ, Poludnenko AY, Hamlington PE (2020) Detonation initiation by compressible turbulence thermodynamic fluctuations. *Combust Flame* 213:172–183
13. Hernández Pérez FE, Mukhadiyev N, Xu X, Sow A, Lee BJ, Sankaran R, Im HG (2018) Direct numerical simulations of reacting flows with detailed chemistry using many-core/GPU acceleration. *Comput Fluids* 173:73–79
14. Desai S, Yu JK, Song W, Luong MB, Hernández Pérez FE, Sankaran R, Im HG (2020) Direct numerical simulations of reacting flows with shock waves and stiff chemistry using many-core/GPU acceleration. *Comput Fluids*, In revision
15. Sankaran R, Im HG, Hawkes ER, Chen JH (2005) The effects of non-uniform temperature distribution on the ignition of a lean homogeneous hydrogen-air mixture. *Proc Combust Inst* 30:875–882

16. Chen JH, Hawkes ER, Sankaran R, Mason SD, Im HG (2006) Direct numerical simulation of ignition front propagation in a constant volume with temperature inhomogeneities: I. fundamental analysis and diagnostics. *Combust Flame* 145:128–144
17. Hawkes ER, Sankaran R, Pébay P, Chen JH (2006) Direct numerical simulation of ignition front propagation in a constant volume with temperature inhomogeneities: II. parametric study. *Combust Flame* 145:145–159
18. Bansal G, Im HG (2011) Autoignition and front propagation in low temperature combustion engine environments. *Combust Flame* 158:2105–2112
19. Gupta S, Im HG, Valorani M (2011) Classification of ignition regimes in HCCI combustion using computational singular perturbation. *Proc Combust Inst* 33:2991–2999
20. Yoo CS, Lu T, Chen JH, Law CK (2011) Direct numerical simulations of ignition of a lean *n*-heptane/air mixture with temperature inhomogeneities at constant volume: parametric study. *Combust Flame* 158:1727–1741
21. Yu R, Bai X-S (2013) Direct numerical simulation of lean hydrogen/air auto-ignition in a constant volume enclosure. *Combust Flame* 160:1706–1716
22. El-Asrag HA, Ju Y (2013) Direct numerical simulations of exhaust gas recirculation effect on multistage autoignition in the negative temperature combustion regime for stratified HCCI flow conditions by using H₂O₂ addition. *Combust Theory Model* 17:316–334
23. El-Asrag HA, Ju Y (2014) Direct numerical simulations of NO_x effect on multistage autoignition of DME/air mixture in the negative temperature coefficient regime for stratified HCCI engine conditions. *Combust Flame* 161:256–269
24. Bhagatwala A, Lu T, Chen JH (2014) Direct numerical simulations of HCCI/SACI with ethanol. *Combust Flame* 161:1826–1841
25. Bhagatwala A, Sankaran R, Kokjohn S, Chen JH (2015) Numerical investigation of spontaneous flame propagation under RCCI conditions. *Combust Flame* 162:3412–3426
26. Bansal G, Mascarenhas A, Chen JH (2015) Direct numerical simulations of autoignition in stratified dimethyl-ether (DME)/air turbulent mixtures. *Combust Flame* 162:688–702
27. Yoo CS, Luo Z, Lu T, Kim H, Chen JH (2013) A DNS study of ignition characteristics of a lean *iso*-octane/air mixture under and SACI conditions. *Proc Combust Inst* 34:2985–2993
28. Luong MB, Luo Z, Lu T, Chung SH, Yoo CS (2013) Direct numerical simulations of the ignition of lean primary reference fuel/air mixtures with temperature inhomogeneities. *Combust Flame* 160:2038–2047
29. Kim SO, Luong MB, Chen JH, Yoo CS (2015) A DNS study of the ignition of lean PRF/air mixtures with temperature inhomogeneities under high pressure and intermediate temperature. *Combust Flame* 162:717–726
30. Luong MB, Yu GH, Chung SH, Yoo CS (2017) Ignition of a lean PRF/air mixture under RCCI/SCCI conditions: a comparative DNS study. *Proc Combust Inst* 36:3623–3631
31. Yu GH, Luong MB, Chung SH, Yoo CS (2019) Ignition characteristics of a temporally evolving *n*-heptane jet in an *iso*-octane/air stream under RCCI combustion-relevant conditions. *Combust Flame* 208:299–312
32. An Y, Jaasim M, Vallinayagam R, Vedharaj S, Im HG, Johansson B (2018) Numerical simulation of combustion and soot under partially premixed combustion of low-octane gasoline. *Fuel* 211:420–431
33. Mittal G, Sung C-J (2006) Aerodynamics inside a rapid compression machine. *Combust Flame* 145:160–180
34. Wang Y, Rutland CJ (2005) Effects of temperature and equivalence ratio on the ignition of *n*-heptane fuel spray in turbulent flow. *Proc Combust Inst* 30:893–900
35. Kokjohn SL, Musculus MPB, Reitz RD (2015) Evaluating temperature and fuel stratification for heat-release rate control in a reactivity-controlled compression-ignition engine using optical diagnostics and chemical kinetics modeling. *Combust Flame* 162:2729–2742
36. Tang Q, Liu H, Yao M (2017) Simultaneous measurement of natural flame luminosity and emission spectra in a RCCI engine under different fuel stratification degrees. *SAE Int J Engines* 10:2017-01-0714

37. Schiebl R, Maas U (2003) Analysis of endgas temperature fluctuations in an SI engine by laser-induced fluorescence. *Combust Flame* 133:19–27
38. Kaiser SA, Schild M, Schulz C (2013) Thermal stratification in an internal combustion engine due to wall heat transfer measured by laser-induced fluorescence. *Proc Combust Inst* 34:2911–2919
39. Söderberg F, Johansson B, Lindoff B (1998) Wavelet analysis of in-cylinder I_{dv} measurements and correlation against heat-release. SAE paper 107:444–456
40. Funk C, Sick V, Reuss DL, Dahm WJA, Turbulence properties of high and low swirl in-cylinder flows, SAE paper (2002) 2002–01–2841
41. Miles PC (2008) Turbulent flow structure in direct-injection, swirl-supported diesel engines. In: *Flow and combustion in reciprocating engines, experimental fluid mechanics*, Springer, pp 173–256
42. Akkerman V, Ivanov M, Bychkov V (2009) Turbulent flow produced by piston motion in a spark-ignition engine. *Flow Turbul Combust* 82:317–337
43. Petersen BR, Ghandhi JB (2010) High resolution scalar dissipation and turbulence length scale measurements in an internal combustion engine. *SAE Int J Engines* 3:65–83
44. Zeldovich YB (1980) Regime classification of an exothermic reaction with nonuniform initial conditions. *Combust Flame* 39:211–214
45. Gu X, Emerson D, Bradley D (2003) Modes of reaction front propagation from hot spots. *Combust Flame* 133:63–74
46. Bradley D, Morley C, Gu XJ, Emerson DR (2002) Amplified pressure waves during autoignition: Relevance to CAI engines. SAE Technical Paper (2002) 2002–01–2868
47. Lee JH, Knystautas R, Yoshikawa N (1978) Photochemical initiation of gaseous detonations. *Acta Astronautica* 5:971–982
48. Lee JHS (2008) *The Detonation Phenomenon*. Cambridge University Press
49. Su J, Dai P, Chen Z (2020) Detonation development from a hot spot in methane/air mixtures: effects of kinetic models. *Int J Engine Res* 146808742094461
50. Gao Y, Dai P, Chen Z (2020) Numerical studies on autoignition and detonation development from a hot spot in hydrogen/air mixtures. *Combust Theo Modell* 24:245–261
51. Bates L, Bradley D, Paczko G, Peters N (2016) Engine hot spots: modes of auto-ignition and reaction propagation. *Combust Flame* 166:80–85
52. Bates L, Bradley D (2017) Deflagrative, auto-ignitive, and detonative propagation regimes in engines. *Combust Flame* 175:118–122
53. Peters N, Kerschgens B, Paczko G (2013) Super-knock prediction using a refined theory of turbulence. *SAE Int J Engines* 6:953–967
54. Dai P, Chen Z, Chen S, Ju Y (2015) Numerical experiments on reaction front propagation in n-heptane/air mixture with temperature gradient. *Proc Combust Inst* 35:3045–3052
55. Yu H, Chen Z (2015) End-gas autoignition and detonation development in a closed chamber. *Combust Flame* 162:4102–4111
56. Dai P, Qi C, Chen Z (2017) Effects of initial temperature on autoignition and detonation development in dimethyl ether/air mixtures with temperature gradient. *Proc Combust Inst* 36:3643–3650
57. Terashima H, Matsugi A, Koshi M (2017) Origin and reactivity of hot-spots in end-gas autoignition with effects of negative temperature coefficients: Relevance to pressure wave developments. *Combust Flame* 184:324–334
58. Pan J, Wei H, Shu G, Chen R (2017) Effect of pressure wave disturbance on auto-ignition mode transition and knocking intensity under enclosed conditions. *Combust Flame* 185:63–74
59. Wei H, Chen C, Shu G, Liang X, Zhou L (2018) Pressure wave evolution during two hotspots autoignition within end-gas region under internal combustion engine-relevant conditions. *Combust Flame* 189:142–154
60. Sow A, Lee BJ, Hernández Pérez FE, Im HG (2019) Detonation onset in a thermally stratified constant volume reactor. *Proc Combust Inst* 37:3529–3536
61. Pan J, Wei H, Shu G, Chen Z, Zhao P (2016) The role of low temperature chemistry in combustion mode development under elevated pressures. *Combust Flame* 174:179–193

62. Pan J, Dong S, Wei H, Li T, Shu G, Zhou L (2019) Temperature gradient induced detonation development inside and outside a hotspot for different fuels. *Combust Flame* 205:269–277
63. Desai S, Sankaran R, Im HG (2019) Unsteady deflagration speed of an auto-ignitive dimethyl-ether (DME)/air mixture at stratified conditions. *Proc Combust Inst* 37:4717–4727
64. Desai S, Sankaran R, Im HG (2020) Auto-ignitive deflagration speed of methane (CH₄) blended dimethyl-ether (DME)/air mixtures at stratified conditions. *Combust Flame* 211:377–391
65. Robert A, Richard S, Colin O, Martinez L, De Francqueville L (2015) LES prediction and analysis of knocking combustion in a spark ignition engine. *Proc Combust Inst* 35:2941–2948
66. Robert A, Richard S, Colin O, Poinot T (2015) LES study of deflagration to detonation mechanisms in a downsized spark ignition engine. *Combust Flame* 162:2788–2807
67. Ali MJM, Luong MB, Sow A, Hernández Pérez FE, Im HG (2018) Probabilistic approach to predict abnormal combustion in spark ignition engines. SAE paper 2018–01–1722
68. Wei H, Chen C, Zhou H, Zhao W, Ren Z (2016) Effect of turbulent mixing on the end gas auto-ignition of *n*-heptane/air mixtures under IC engine-relevant conditions. *Combust Flame* 174:25–36
69. Chen L, Wei H, Chen C, Feng D, Zhou L, Pan J (2019) Numerical investigations on the effects of turbulence intensity on knocking combustion in a downsized gasoline engine. *Energy* 166:318–325
70. Zhong L, Liu C (2019) Numerical analysis of end-gas autoignition and pressure oscillation in a downsized SI engine using large eddy simulation. *Energies* 12:3909
71. Zhang T, Sun W, Wang L, Ju Y (2019) Effects of low-temperature chemistry and turbulent transport on knocking formation for stratified dimethyl ether/air mixtures. *Combust Flame* 200:342–353
72. Nogawa T, Terashima H (2020) Effects of globally stratified temperature distributions and NTC characteristics on end-gas combustion modes. *Combust Sci Technol* 1–25
73. Wang L, Peters N (2006) The length-scale distribution function of the distance between extremal points in passive scalar turbulence. *J Fluid Mech* 554:457–475
74. Pal P, Valorani M, Arias PG, Im HG, Wooldridge MS, Ciottoli PP, Galassi RM (2017) Computational characterization of ignition regimes in a syngas/air mixture with temperature fluctuations. *Proc Combust Inst* 36:3705–3716
75. Luong MB, Lu T, Chung SH, Yoo CS (2014) Direct numerical simulations of the ignition of a lean biodiesel/air mixture with temperature and composition inhomogeneities at high pressure and intermediate temperature. *Combust Flame* 161:2878–2889
76. Luong MB, Yu GH, Lu T, Chung SH, Yoo CS (2015) Direct numerical simulations of ignition of a lean *n*-heptane/air mixture with temperature and composition inhomogeneities relevant to HCCI and SCCI combustion. *Combust Flame* 162:4566–4585
77. Zhang J, Luong MB, Hernández Pérez FE, Han D, Im HG, Huang Z (2019) Exergy loss of dme/air mixtures and ethanol/air mixtures with temperature and concentration fluctuations under HCCI/SCCI conditions: a DNS study, submitted to proceedings of the combustion institute (2019)
78. Luong MB, Yu GH, Chung SH, Yoo CS (2017) Ignition of a lean PRF/air mixture under RCCI/SCCI conditions: chemical aspects. *Proc Combust Inst* 36:3587–3596
79. Luong MB, Sankaran R, Yu GH, Chung SH, Yoo CS (2017) On the effect of injection timing on the ignition of lean PRF/air/EGR mixtures under direct dual fuel stratification conditions. *Combust Flame* 183:309–321
80. Echekeki T, Chen JH (2003) Direct numerical simulation of autoignition in non-homogeneous hydrogen-air mixtures. *Combust Flame* 134:169–191